Research Square

Preprints are preliminary reports that have not undergone peer review.
They should not be considered conclusive, used to inform clinical practice,
or referenced by the media as validated information.

Acute lung injury induces sustained neuroinflammation and dysfunction in the brainstem nucleus of the solitary tract of rats

Stuart B. Mazzone
University of Melbourne
Alexa R. Prawduik
University of Melbourne
Robert Behrens
University of Melbourne
Kathryn S. Stok
University of Melbourne
Robert J. O'Donoghue
University of Melbourne
Gary P. Anderson
University of Melbourne
Eloise M. Whitehead
University of Melbourne
Tara G. Bautista
University of Melbourne
Matthew W. Trewella
University of Melbourne
Alice E. McGovern
alice.mcgovern@unimelb.edu.au
University of Melbourne

Research Article

Keywords: lung fibrosis, nucleus of the solitary tract, neuroinflammation, vagal reflexes, neuroimmune signalling, lung-brain axis, bleomycin

Posted Date: May 25th, 2026

DOI: https://doi.org/10.21203/rs.3.rs-9685636/v1

License: This work is licensed under a Creative Commons Attribution 4.0 International License.
Read Full License

Additional Declarations: No competing interests reported.

Version of Record: A version of this preprint was published at Journal of Neuroinflammation on October 12th, 2026. See the published version at https://doi.org/10.1186/s12974-026-04079-5.

Abstract

Background

Acute lung injury (ALI) causes profound pulmonary inflammation and is increasingly associated with neurological symptoms, suggesting that inflammatory signalling extends beyond the lungs to affect central nervous system circuits. However, the molecular and functional consequences of ALI in brainstem regions involved in respiratory control remain poorly defined. Here, we examined the impact of bleomycin-induced ALI on the nucleus of the solitary tract (NTS), the primary brainstem termination site of vagal sensory afferents from the lungs.

Main body:

Using a rat model, a single intratracheal dose of bleomycin (7.5 mg/kg) induced acute lung inflammation, persistent tissue pathology, and altered respiratory parameters lasting up to 28 days. Transcriptomic profiling of the NTS revealed widespread gene expression changes at both day 7 and day 28. Ranked gene set enrichment analysis showed that early transcriptional changes were characterised by positive enrichment of synaptic signalling and neurotransmission-related processes, together with negative enrichment of metabolic, lipid catabolic, and immune-associated pathways. By day 28, positively enriched pathways shifted towards mitochondrial and energy-generating processes, whereas negatively enriched pathways implicated synaptic organisation, neuronal guidance, and cell adhesion-related biology. Morphometric analysis of IBA1-positive microglia demonstrated significant changes in microglial morphology within the NTS at both time points, consistent with a reactive phenotype. Functionally, *in vivo* microinjections of capsaicin or glutamate analogues into the NTS evoked significantly attenuated respiratory reflex responses in bleomycin-treated rats compared with controls.

Conclusion

Bleomycin-induced ALI drives sustained neuroinflammatory and functional disruption in the NTS, a key brainstem hub for pulmonary vagal signalling. These findings provide new evidence for lung-to-brain communication in ALI and identify molecular pathways that may underlie impaired reflex control and broader neurological morbidity associated with respiratory disease.

Introduction

Acute lung injury (ALI) is a major contributor to human morbidity, resulting from direct insults such as lung infections or non-pathogenic exposures, or indirect factors including systemic inflammation. Regardless of the cause, ALI is characterised by profound pulmonary inflammation that drives widespread tissue damage, structural remodelling and in some cases advancing fibrosis. These pathological changes compromise respiratory function and can escalate into acute respiratory distress

syndrome (ARDS). Central to this inflammatory cascade is the activation of the airway epithelium, recruitment of immune cells, and an upregulation of pro-inflammatory mediators, including tumour necrosis factor alpha (TNFa), interleukin 1 beta (IL-1b) and IL-6 which act on a variety of lung-resident cells to contribute to tissue pathology (1–4).

ALI is typically associated with an array of symptoms, including altered perceptions of breathing adequacy (dyspnoea), abnormal breathing patterns, cough, lethargy and other changes in behaviour. This pattern of symptoms is consistent with the idea that inflammatory processes in the lung can disrupt normal nervous system function. Indeed, several preclinical animal studies have shown a range of neurological pathologies accompanying ALI, ranging from neuroinflammatory changes in the vagal nerves that innervate the airways and lungs (5–9), to alterations in the brainstem nuclei that are involved in regulating vagal nerve function (10–15), and even dysfunction in higher brain regions (16–24). In our previous work using an influenza-based model of ALI, we found that the vagal sensory ganglia, the site housing the cell bodies of lung-projecting sensory neurons, exhibited marked increases in inflammatory cell infiltration during infection. This immune cell expansion was accompanied by significant transcriptional reprogramming, including the upregulation of genes associated with innate antiviral defence. Notably, this response was not triggered by direct viral infection of the vagus nerve but was instead replicated by introducing non-infectious viral mimetics or inflammatory mediators into the lungs. These findings implicate lung-derived inflammatory mediators, acting through a neuroimmune signalling axis, as key drivers of vagal neuroinflammation (6).

Further evidence for neuroimmune-driven neuroinflammation in ALI comes from non-pathogenic models. For example, lung instillation of bleomycin, a chemotherapeutic drug that induces lung injury, was shown to activate microglial cells (the brain's resident immune cells) in the region of the nucleus of the solitary tract (NTS) in the brainstem (13, 14). The NTS is the primary central termination site of vagal sensory nerve fibres (25, 26), implicating propagation of inflammation along sensory neural pathways from the vagus nerve to the brainstem during ALI. The full characteristics and functional consequences of this neuroinflammation are not fully described, although *ex vivo* electrophysiological studies of brainstem slices from young rats previously exposed to bleomycin reveal altered synaptic communication between vagal sensory nerves and NTS neurons (11). Collectively, ALI-induced neuroinflammation may compromise functioning along these sensory neural pathways, potentially contributing to the myriad of neurological symptoms observed in patients with ALI (27, 28). Because the NTS integrates pulmonary vagal sensory input and contributes to autonomic and respiratory reflex control, inflammatory disruption of this region could have important consequences for both breathing and broader sickness-related behaviours.

In this study, we set out to deepen our understanding of how non-pathogenic ALI shapes brainstem neuroinflammation. Specifically, we investigated the transcriptional landscape and functional consequences of bleomycin-induced lung injury on the brainstem NTS, shedding light on how lung inflammation may alter brainstem circuit function.

Materials and Methods

Animals

This study complies with the *Australian Code for the Care and Use of Animals for Scientific Purposes* from the National Health and Medical Research Council (NHMRC) of Australia. All procedures were approved by the Animal Ethics Committee of the University of Melbourne, Australia (approval number 2022-20038-25119-8). All steps were taken to minimise the animals' pain and suffering, as mandated in the above Australian Code. Sprague-Dawley male and female rats between 8–12 weeks of age (200–300 g) were housed with 12 h light/dark cycles with access to food and water *ad libitum*. Rats were divided into two main groups, vehicle-treated (control) and bleomycin-treated and housed in groups of up to four according to their treatment (vehicle or bleomycin) and termination time point (days 7 and 28 post instillation).

Bleomycin instillation and tissue analysis

Rats received a single intratracheal (i.t.) dose of bleomycin sulphate (Cayman Chemical, Michigan, USA) at 7.5 mg/ kg prepared in sterile saline. Vehicle-treated animals received the equivalent volume of sterile saline only. Rats were anaesthetised with isoflurane (4% induction and 2% maintenance in oxygen) via a nose cone and placed supine on an incline board. Once their withdrawal and palpebral reflexes had disappeared a midline incision was made on the ventral surface of their neck to expose the larynx and trachea. Rats received an injection of either bleomycin or saline, slowly (over 1 minute) into the tracheal lumen (~ 5–6 cartilage rings below the larynx) via a 1 ml syringe connected to a 30 G needle. The injectate was followed by an immediate puff of air, to aid in optimal distribution of the solution. The incision was sutured, and animals were allowed to recover for either 7 or 28 days during which body weight was monitored and recorded daily and post-operative analgesics administered for 48 hours (meloxicam, 5 mg/ kg and buprenorphine 0.05 mg/ kg s.c., b.i.d.).

Whole-body plethysmography recordings

Respiratory parameters were measured in rats using calibrated 4-chamber unrestrained whole-body plethysmography (WBP, Buxco, Wilmington, USA). Rats were acclimatised to the plethysmography chambers (30 minutes per day) each day for 3 days prior to experimentation. Respiratory frequency (f, breaths min^{-1}), tidal volume (TV, ml kg^{-1}), minute volume (MV, ml min^{-1}), inspiratory and expiratory time (Ti and Te, sec), estimated peak inspiratory and expiratory flow (PIF and PEF, ml sec^{-1}), pause and enhanced pause (PAU and Penh, arbitrary unit of measure), expiratory flow at 50% expired volume (EF50, ml sec^{-1}), the location into expiration where the peak occurs as a fraction of Te (Rpef), relaxation time (Tr, sec), duration of breaking – the percentage of breath occupied by transitioning from inspiration to expiration (TB), and duration of pause before expiration – percentage of breath occupied by transition from expiration to inspiration (TP) were automatically sampled from the calibrated Buxco flow trace,

corrected for animal body weight and ambient chamber temperature, and calculated in real time by the plethysmography software (Buxco Finepointe Software Version 2.1.0.9). Real time data collected every 2 sec were used to calculate the average per 20 min for each animal at baseline (day 0, prior to instillation), and 7- and 28- days post-instillation. Data was normalised to baseline values for each animal. Normalisation was performed to remove confounding factors such as inter-animal variation in baseline parameters.

Physiological studies in anaesthetised rats

Rats were anaesthetised with urethane (1.5 g/ kg, i.p.), the level of which was determined to be adequate by assessing the palpebral and limb withdrawal reflexes. Animals were placed supine on a thermostatically controlled heating pad set at 36.5°C and body temperature maintained via feedback from a rectal probe. A midline incision was made along the ventral surface of the neck to expose the trachea and underlying nerves and blood vessels. The left carotid artery was cannulated using polyethylene tubing (internal diameter = 0.5 mm, outer diameter = 0.9 mm) attached to a pressure transducer filled with heparinised saline (50 U/ ml, Sigma Aldrich) to measure arterial blood pressure. The distal extrathoracic trachea was cannulated and connected via a side port to a pressure transducer to measure the tracheal pressure and changes associated with spontaneous respiration. Output from pressure transducers was digitised and recorded (LabScribe, iWorx, USA). Rats were then placed onto a stereotaxic frame (Model 940, David Kopf Instruments, USA) and to access the medulla the head was angled ~ 45° with a midline incision made through the animal's skin, posterior neck muscles, and dura mater between the occipital bone and C1 vertebra. Using obex as a reference point (~0.5 mm rostral to the calamus scriptorius), microinjections of either capsaicin (0.01, 0.1, 1 μM; 150 nl; Sigma Aldrich, Australia) or L-glutamic acid (0.1, 1, 10 mM; 150 nl; Sigma Aldrich, Aus) were made into the caudal NTS (0 mm level to obex, 0.3 mm lateral to the midline, and 0.5 mm below the medullary surface) or paratrigeminal nucleus (Pa5; 0.3 mm rostral to obex, 2–3 mm lateral to midline, and 0.5 mm below the medullary surface) (29). Respiration and blood pressure parameters were recorded for 30 or 10 min post capsaicin or L-glutamic acid microinjection, respectively.

Tissue sampling and analyses

All tissue samples were obtained from rats that were euthanised post-instillation with sodium pentobarbital (100 mg/ ml) and either exsanguinated or transcardially perfused with PBS; 0.1 M, pH 7.45, followed by 4% PFA; pH 7.45.

Broncho-alveolar lavage fluid (BALF) total cell counts

Aspirated BALF was collected via the trachea and clarified by centrifugation with red blood cells (RBC) lysed in RBC lysis buffer (0.15 M NH_4Cl, 17 nM Tris-HCl at pH 7.2, sterile filtered) for 1 min and cell pellet

resuspended in 0.1M PBS. Total cell counts were performed on an automated cell counter (Countess 3, Invitrogen, Aus).

Lung collagen assay

Total lung collagen levels were determined via an alkaline hydrolysis assay (Abcam; ab222942) on lung lysates according to the manufacturer's instructions and read with CLARIOstar Plus (BMG labtech) microplate reader.

RNA extraction

Lungs and nucleus of the solitary tract (NTS) brain samples were freshly harvested, placed in 500 µl TRIzol reagent (Qiagen), snap frozen and stored at -80°C until further processing. Thawed samples were homogenised and RNA was extracted and concentrated using the RNeasy MiniElute Cleanup kit (Qiagen) according to the manufacturer's instructions.

qPCR analysis of lung samples

cDNA was generated using the high-capacity cDNA reverse transcription kit (Life technologies) and random primers (host RNA) according to the manufacturer's instructions. Real-time PCR was performed on generated cDNA with SYBR Green using QuantStudio 6 Real-Time PCR (ThermoFisher Scientific). Lung inflammatory genes of interest included Tumour necrosis factor a (*Tnfa*; forward primer- CTCACACTCAGATCATCTTC, reverse primer- GAGAACCTGGGAGTAGATAAG), Interleukin 4 (*Il4;* forward primer- GAACCAGGTCACAGAAAAAG, reverse primer- GGGAAGTAAAATTTGCGAAG), and Interleukin 6 (*Il6*; forward primer- CAGAGTCATTCAGAGCAATAC, reverse primer- CTTTCAAGATGAGTTGGATGG). Lung pro-fibrotic genes of interest included Collagen type 1 alpha 1 chain (Col1a1; forward primer- TGGATTCCAGTTCGAGTATG, reverse primer- AGTGATAGGTGATGTTCTGG), Collagen type 1 alpha 2 chain (*Col1a2*; forward primer- AGTGGAAGAGCGATTACTAC, reverse primer- ATTGATGGTCTCTCCTAACC), and connective tissue growth factor (*Ctgf*, forward primer- AAACTGATAGCCTCAAACTC, reverse primer- ACTTCTGATCCATTGCTTTAC). Gene expression was normalised relative to Hypoxanthine phosphoribosyl transferase (*Hprt;* forward primer- ACTGGTAAAACAATGCAGAC, reverse primer- CCTGAAGTGCTCATTATAGTC) and Mitogen-activated protein kinase 14 (*Mapk14;* forward primer -CAACCAGACAGTGGATATTTG, reverse primer- CTGTTAATGAGATAAGCAGGG) expression. Fold change was calculated based on the $2^{\Delta\Delta CT}$ method.

RNA sequencing and analysis

Library preparation and sequencing was performed on NTS brain samples by Australian Genome Research Facility (AGRF, Melbourne, Australia). Briefly, RNA sequencing libraries were generated using the Illumina TruSeq RNA sample preparation according to the manufacturer's instructions. RNA sequencing was performed using the Illumina NovaSeq X Plus platform on 150 bp paired end reads. The

primary sequence data was generated using the Illumina DRAGEN BCL Convert 07.021.645.4.0.3 pipeline with FastQ files generated. The cleaned sequence reads were then aligned against the genome. The STAR aligner (v2.3.5a) was used to map reads to the genomic sequences. Sequencing quality was assessed using standard AGRF quality-control summaries. Across samples, total reads per sample ranged from approximately 21.8 to 38.3 million, with 76.4–80.9% of paired reads mapping to the genome and 57.7–64.2% mapping to annotated features (Table S1). Sample-level quality control was further assessed after normalisation by inspection of multi-dimensional scaling plots, and no outlier samples were excluded from downstream analysis.

edgeR (version 4.0.9) was used for count normalisation in R 4.3.1 using the default TMM method. Differential expression analysis was carried out using a limma-voom pipeline (30, 31) to compare NTS samples from vehicle- and bleomycin-treated rats, with significance defined at an adjusted *p*-value threshold of 5%. For heatmap visualisation (Fig. 2), mean-adjusted logCPM values of the top 100 differentially expressed genes were averaged across biological replicates, and genes (rows) were ordered by log-fold-change between groups. Ranked gene set enrichment analysis (GSEA) of Gene Ontology biological process (GO:BP) categories was performed using WebGestalt (32). For each time point, the full ranked gene list generated from the limma-voom output was used as input, with gene-wise moderated t-statistics used as the ranking metric. Enrichment was assessed against GO:BP gene sets for *Rattus norvegicus*, and terms were considered significant at FDR < 0.05. Figure 2 shows the selected top 10 positively enriched and top 10 negatively enriched GO:BP terms displayed according to normalised enrichment score (NES). Full differential expression tables from the limma-voom analysis (Tables S2-S3, respectively) are provided in the supplementary material, together with the full Gene Ontology biological process (GO:BP) ranked gene set enrichment analysis (GSEA) output tables for day 7 and day 28 (Tables S5-S6, respectively).

Lung microCT scanning

Insufflated lungs fixed with 4% PFA were incubated for 4 hours each in 80 and 90% ethanol and then overnight in 100% ethanol. Lungs were subsequently transferred to 100% hexamethyldisilazane for 3 hours, prior to air-drying. Lungs were packaged for micro-CT scanning and scanned on a microCT50 (Scanco Medical AG, Bruttisellen, Switzerland) with no filter at an energy of 45 kVp, intensity of 200 uA, integration time of 400 ms, and a voxel resolution of 17.2 mm.

MicroCT image analysis

Lung injury was quantified using a supervised machine learning based analysis approach. Tissue segmentation analysis was performed using ilastik (version 1.4.0; (33)). Briefly, the program was trained on vehicle (control)- and bleomycin-treated lungs to recognise 'features' such as injured (fibrotic)/ healthy tissue, alveolar space, vessels, and cartilage. The distinct data from each feature was then exported into IMARIS (RRID:SCR_007370) as separate channels where the volume of voxels from the injured channel was divided by the total tissue volume (all channels merged) to calculate the percentage of fibrotic lung volume.

Immunofluorescence

Medullary brainstems were removed from transcardially perfused rats and post-fixed in 4% PFA (overnight) then cryoprotected in 30% sucrose (w/v PBS, 48 hours) before freezing in Optimal Cutting Temperature compound (OCT, TissueTek). 30 µm cryostat-cut sections of rat brainstems encompassing the NTS and Pa5 region were collected serially into 0.1 M PBS and processed for immunohistochemistry that same day. All sections were rinsed in PBS then blocked in 10% donkey serum in 0.1 M PBS for 1 hr, before incubation for 24 hours in the primary antibody of interest: Rabbit anti-NeuN, 1:500, Abcam, ab177487; Goat anti-IBA1, 1:500, Abcam, ab5076. All antibodies were diluted in antibody diluent (2% donkey serum and 0.3% Triton X-100 in PBS). After the required incubation, sections were washed three times with PBS for 10–20 mins each then incubated for one hour in appropriate Alexa-Fluor fluorescently-conjugated secondary antibodies (1:500, ThermoFisher Scientific, Aus). Brainstem sections were kept in order and mounted onto gelatin-coated slides. All slides were coverslipped with an antifade mounting media containing DAPI (ProLong Gold, ThermoFisher Scientific, Aus).

Microscopy and analysis

Brainstem sections were imaged on a Zeiss Axioscan 7 slice scanner at x20 magnification at the same exposure for each protein of interest across each sample for offline analysis. Counts of IBA1 cells were manually performed in the NTS along the rostrocaudal spread spanning − 1600 µM to + 1100 µM, and the Pa5 along the rostrocaudal spread spanning − 480 µM to 1100 µM, relative to obex. For microglia, single cell fractal and skeletal analysis were performed using the method described by (34) on randomly selected cells from the NTS and Pa5 at the level of -0.24 mm and + 0.3 mm, relative to obex, respectively. Briefly, using Fiji (35), the image containing the brain region of interest underwent processing, converted to binary and a region of interest (ROI) was sized to fit around all the microglia analysed in this study to ensure the scale remained the same. A random number generator was used to determine x, y coordinates to randomly select 15 microglia per brain region of interest. Each microglial cell was selected with the ROI, duplicated and processed individually. Using the original image as reference, the paintbrush tool was employed to remove any fragments not associated with the microglia of interest and to connect branches that had become disconnected due to the pre-processing procedure. The final binary image was converted to an outline and the FracLac plugin was used to analyse each cell. Fractal dimension, lacunarity, circularity, maximum span across hull, area and perimeter were measured. The microglia used for fractal analysis were converted to a skeleton image and analysed using the AnalyzeSkeleton (2D/3D) plugin in ImageJ. Number of branches and junctions, longest to shortest path, average and total branch length were measured. The 15 technical replicates of microglia measurements taken from one animal were averaged. This mean value was then used for statistical comparisons between the vehicle and bleomycin-treated groups.

High resolution digital images taken at 200x magnification were imported into Adobe Photoshop (version 20.0.4) and optimised (minimally) for brightness, contrast, and size for preparation of representative photomicrographs.

Statistical analysis

Statistical analyses (not including the RNASeq) were performed using GraphPad Prism, version 10.4.0 for Mac (GraphPad Software, CA, USA). Data are expressed as the mean ± SEM, with statistical significance set as $p \leq 0.05$, unless stated differently. Normal (gaussian) distribution of test groups was determined using Shapiro-Wilk's test. If samples didn't meet normality assumptions, the relevant nonparametric statistical test was used. Statistical test and significance were determined as described in the figure legends and/ or text.

Results

Model characterisation

A single intratracheal instillation of bleomycin (7.5 mg/kg, day 0) resulted in an initial reduction in body weight peaking at approximately day 4 following bleomycin treatment, followed thereafter by progressive body weight gain over the 28-day experimental period, albeit lagging vehicle control animals at all measured time points (Fig. 1B). Bleomycin induced an acute inflammatory response in the lungs observed at day 7 which consisted of an increase in lung to body weight ratio (Fig. 1C), an increase in the total number of cells in the bronchoalveolar fluid (Fig. 1D) and a significant increase in inflammatory genes *Tnfa, Il4* and *Il6* (Fig. 1E). By day 28, these measures had returned to levels similar to vehicle controls. The single bleomycin challenge led to a marked elevation in collagen deposition within the lungs, evidenced by increased hydroxyproline levels observed on day 28 (Fig. 1F). The expression of genes associated with fibrotic markers: *Col1a1, Col1a2* and *Ctgf* peaked at day 7 and showed a subsequent reduction by day 28, however, their levels remained significantly higher compared to vehicle control groups (Fig. 1G). High-resolution *ex vivo* whole lung micro-CT imaging with unbiased automated machine learning quantitation revealed significant lung injury as early as day 7, characterised by approximately 18% of the total lung volume presenting with abnormal tissue signal on CT volumes (Fig. 1H). The microCT signal of lung injury remained substantially elevated at day 28 compared to vehicle controls (Fig. 1H). The pathological impacts following bleomycin-induced ALI were accompanied by disordered respiratory function at both day 7 and day 28. In whole body plethysmography, bleomycin-treated rats exhibited significant changes in respiratory parameters which included an increase in frequency (both inspiratory and expiratory time were reduced, Table E1), a reduction in tidal volume, an increase in Penh and EF50, compared to vehicle-treated controls, indicative of respiratory distress (Fig. 1I). Changes in other respiratory parameters were observed including Rpef and relaxation time (Tr) (Table E1).

Table E1

Respiratory parameters in vehicle- and bleomycin-treated rats, measured via whole body plethysmography.

	Day 7		Day 28	
	Vehicle	**Bleomycin**	**Vehicle**	**Bleomycin**
Respiratory rate	3.8 ± 3.6	72.1 ± 7.7****	-3.1 ± 4.3	37.8 ± 7.7**
Tidal volume	20.1 ± 4.4	-16.2 ± 3.6****	34.3 ± 5.8	23.1 ± 8.0
Minute volume	23.6 ± 4.9	40.0 ± 5.9	29.8 ± 4.8	70.5 ± 16.0**
Enhanced Pause	-3.1 ± 4.5	35.4 ± 9.8	-3.0 ± 7.2	64.3 ± 25.8**
Pause	1.0 ± 2.1	20.4 ± 7.2	0.1 ± 5.1	58.1 ± 27.0**
Rpef	0.6 ± 3.9	-7.9 ± 2.8	0.6 ± 6.0	-21.5 ± 4.6**
Peak inspiratory flow	27.3 ± 6.4	27.5 ± 5.5	35.3 ± 7.0	76.2 ± 23.9*
Peak expiratory flow	19.2 ± 4.3	49.0 ± 6.7*	26.7 ± 4.8	82.6 ± 22.0**
Inspiration time	-2.6 ± 3.2	-33.1 ± 2.9****	5.6 ± 4.2	-22.7 ± 4.4****
Expiration time	0.2 ± 2.6	-39.6 ± 3.0****	9.9 ± 5.0	-21.1 ± 4.6****
Ejection fraction 50 (EF50)	18.8 ± 4.7	70.1 ± 9.1**	25.4 ± 5.9	97.7 ± 25.8**
Relaxation time (Tr)	-0.2 ± 2.3	-43.4 ± 3.0****	7.1 ± 4.3	-31.7 ± 4.9****
Duration of breaking (TB)	-9.8 ± 7.4	6.6 ± 5.6	-4.8 ± 8.0	-14.8 ± 6.1
Duration of pause before exp (TP)	-4.7 ± 6.0	29.1 ± 6.4***	-2.5 ± 10.1	-9.2 ± 6.7

Data are normalised to baseline levels and presented as mean ± SEM. *, **, **** denotes significance of $p < 0.05$, $p < 0.01$, $p < 0.0001$, respectively, as corrected for multiple comparisons and determined by mixed effects model (Šídák).

Bleomycin-induced transcriptional changes in the nucleus of the solitary tract

Bulk RNAseq transcriptional analysis performed on the NTS from rats assessed the number of differentially expressed genes (DEGs) 7- and 28-days following bleomycin-treatment compared to vehicle-treated control animals (Fig. 2; Tables S2-S3). The variation of differentially expressed genes across each sample can be seen via multidimensional scaling analysis with vehicle- and bleomycin-treated cohorts clearly separated (Fig. 2A (7 days), E (28 days)). At day 7 post-bleomycin treatment, a total of 4411 DEGs were identified: 2223 upregulated and 2188 downregulated. Bleomycin-induced

differential gene expression persisted at day 28 post-treatment with a total of 1246 DEGs identified: 584 upregulated and 662 downregulated (Fig. 2B-G). 421 DEGs were common across the two time points (Table S4). Ranked gene set enrichment analysis of the full NTS transcriptome refined the pathway-level interpretation at both time points (Fig. 2D, H; Tables S5-S6). At day 7, positively enriched GO:BP terms were dominated by synaptic and neuronal signalling processes, including synaptic transmission, vesicle-mediated transport in synapse, neurotransmitter transport, regulation of membrane potential, and neuron cellular homeostasis, whereas negatively enriched terms included fatty acid and lipid catabolic processes, small molecule catabolism, antigen processing and presentation, and interleukin-associated processes. At day 28, positively enriched pathways shifted toward mitochondrial and metabolic programs, including NADH dehydrogenase complex assembly, mitochondrial gene expression, precursor metabolite generation, proton transmembrane transport, and redox homeostasis, while negatively enriched pathways implicated synaptic organisation, glutamatergic signalling, neuronal guidance, and cell adhesion-related processes.

Bleomycin-induced microglial changes in the nucleus of the solitary tract

Quantitation of IBA1 immunostained microglia across the rostrocaudal extent of the NTS showed that the total number of microglial cells was not significantly altered by bleomycin-treatment compared to vehicle-treated controls at either day 7 or day 28 (Fig. 3A). However, microglial morphology appeared altered by bleomycin treatment (Fig. 3B-E) suggesting changes in microglial reactivity. Fractal dimension was significantly reduced at day 7, and lacunarity trended downwards, indicating a loss of complexity and more homogeneous cell architecture. Significant reductions in geometric measures including area, perimeter, and maximum span across the convex hull further supported process retraction at days 7 and 28, while circularity remained unchanged (Fig. 3D). Skeletal analysis showed significantly fewer branches and junctions, reduced total branch length, and shorter maximal path lengths at both days 7 and 28, with no significant change in average branch length, indicating that while the number of processes decreased, the remaining branches were not substantially shorter. These findings indicate a shift toward a less ramified, reactive microglial phenotype sustained across both time points. These changes were observed in microglia within the NTS, a key brainstem region receiving lung vagal afferents. In contrast, no significant morphometric changes were detected in microglia from the paratrigeminal nucleus (Pa5), a medullary brainstem region that also receives a subset of lung vagal afferents (36), suggesting region-specific microglial reactivity to bleomycin-induced lung injury (Figure E1).

Bleomycin-induced function changes in the nucleus of the solitary tract

In urethane anesthetised rats, baseline respiratory rate at day 28 was slightly higher in bleomycin-treated rats compared to vehicle-treated control rats (143.3 ± 15.8 vs. 116.4 ± 7.0, respectively), however, this

difference was not statistically significant (p = 0.1366). The activation of the central terminals of vagal sensory nerve fibres in the NTS via bilateral microinjections of capsaicin (Fig. 4A) produced a characteristic decrease in respiratory frequency in vehicle-treated control rats. The peak effect of capsaicin microinjections approached a complete apnoea within 2 mins and was followed by a progressive recovery in breathing frequency to baseline levels within 10–12 mins (Fig. 4B-D). By contrast, comparable studies at day 28 in bleomycin-treated rats showed an attenuated respiratory response to capsaicin microinjection. Thus, although the peak effect of capsaicin similarly occurred within 2 mins of microinjection, the magnitude and duration of the evoked reduction in respiratory frequency was significantly less (Fig. 4B-D). Consequently, an analysis of the total area under the capsaicin-evoked respiratory response curve showed a highly significant reduction in functional responsivity for all doses of capsaicin tested (Fig. 4D). Bilateral NTS microinjections of the L-glutamic acid (LGA), an activator of postsynaptic NTS neurons, mimicked the respiratory effects of capsaicin in vehicle-treated animals. Again, LGA-evoked responses were significantly blunted in bleomycin-treated rats (Fig. 4E). Functional experiments were not feasible at day 7 due to the impact of bleomycin treatment on general animal health at this stage of the model. In parallel experiments assessing respiratory responses to capsaicin and LGA, microinjections into the Pa5 reduced respiratory frequency (29), however, no differences were observed between vehicle- and bleomycin-treated animals suggesting that the functional impacts of bleomycin are likely confined to the NTS (Figure E2).

Discussion

ALI is often accompanied by a spectrum of neurological complications, suggesting that lung inflammation can influence neural circuit function. In this study we investigated the neuroinflammatory and functional consequences of ALI in the rat NTS, a key brainstem site that receives input from vagal pulmonary sensory nerves capable of detecting lung inflammation. Our findings demonstrate that bleomycin-induced ALI leads to pronounced transcriptional and microglial changes in the NTS, detectable at 7 days post-induction and persisting for at least 28 days. These molecular and cellular changes were accompanied by impaired NTS function, as *in vivo* respiratory physiological studies showed that respiratory reflex responsivity evoked from the region of the caudal NTS was blunted during this period. Together, these data support the notion that lung injury and inflammation have a range of impacts on distant neural tissues and provide a framework for understanding the neurological symptoms that frequently accompany respiratory disease. More broadly, our findings align with emerging evidence for a lung-brain axis in acute lung injury, including studies implicating vagus nerve-dependent CNS pathology, barrier dysfunction, and neurocognitive impairment (23, 24).

ALI and neuroinflammation

The chemotherapeutic agent bleomycin is commonly used in preclinical studies to induce tissue injury for investigating acute and persistent organ pathologies. When administered to the lung, it elicits a rapid induction of pulmonary inflammation which, with repeated dosing, can progress to consolidated fibrotic lung scarring. Consequently, bleomycin has been used extensively to model ALI and pulmonary fibrosis

in laboratory animals (37–40). Our current studies employed a single, moderate dose of bleomycin which was sufficient to induce a sustained lung pathology that persisted for at least 28 days. While animals initially lost body weight and demonstrated elevations in multiple inflammatory markers, fibrotic gene expression, collagen deposition and other pathological changes in lung tissue contributing to deficits in basal respiratory parameters, these effects were generally more pronounced at earlier than later time points. This is consistent with our assertion that the model more accurately reflects an acute lung injury rather than a persistent fibrotic lung disease.

Our current data support and build upon previous studies showing that lung injury and inflammation can impact neural circuits involved in respiratory control. This influence is best characterised as a neuroinflammatory neuropathology, marked by molecular and cellular signs of inflammation across both peripheral and central components of the nervous system. Pulmonary exposures to infectious pathogens, bacterial and viral mimetics and allergens have all been shown to increase inflammatory cell numbers in the vagal sensory ganglia and drive gene expression profiles consistent with active tissue neuroinflammation (5–9). Several studies have also reported evidence for brainstem and broader brain regional inflammation following pathogenic and non-pathogenic lung insults, including microglial activation and altered expression of inflammatory mediators or their corresponding genes (13, 14, 16, 18, 20, 41, 42).

To our knowledge, this is the first study to provide a comprehensive analysis of the molecular characteristics of brainstem neuroinflammation, revealing widespread gene expression changes in the NTS following lung bleomycin exposure, as demonstrated by our RNA sequencing data. Assessment of the most significant DEGs identified at day 7 following the induction of ALI, suggests the establishment of an initial inflammatory and injurious microenvironment within the NTS. Notably, upregulation of genes associated with inflammation and cellular injury, (*Pde10a, Tial1, Wsb1*) and downregulation of genes associated with cell protection (*Prdx6, Dao, Vsir, Lrrc8d*) characterise this early phase of neuropathology. PDE10A, a dual cAMP/cGMP hydrolysing enzyme, is of considerable interest given prior studies showing that PDE10A inhibition reduces acute brain injury and improves neuropathic pain (43–45), while PRDX6 and DAO have well defined roles in combatting oxidative stress and detoxifying D-serine, respectively in the brain (46–49). *Lrcc8d* encodes an essential volume-activated anion channel, and its downregulation impacts cell volume regulation leading to cytotoxicity (50). The presence of microglia already displaying the structural characteristics of activation at this early time point reaffirms the neuroinflammatory state. Day 7 of ALI was also characterised by the upregulation of several genes associated with neurotransmission (*Unc80, Gria2, Nos1ap*), downregulation of genes involved in normal metabolic function (*Acsbg1, Cpt2, Kcnj16*) and disordered expression of a variety of genes involved in regulating neural structure, including actin, neurofilament and microtubule regulation (*Ssh, Sacs*), cell growth (*Rictor*) and neurite/ axonal maintenance (*Ncan, Psd2)*. Interestingly, an upregulation of *Col19a1* at day 7 suggests changes in the extracellular matrix may also contribute to any structural abnormalities present. This pathway-level interpretation was reinforced by ranked gene set enrichment analysis, which showed that day 7 transcriptional changes were characterised by positive enrichment of synaptic and

neurotransmission-related processes and negative enrichment of lipid catabolic, small-molecule metabolic and immune-associated pathways.

By day 28 following bleomycin treatment, the changes in the transcriptional landscape in the NTS suggest an advancement in presentation of the ALI associated neuropathology. At this time point, many of the topmost significant DEGs were downregulated in expression. This included genes associated with neuroprotection (*Prom1, Flt1*), normal regulation of inflammation (*Adgrf5, Itm2a, Nbeal2*) and the negative regulation of apoptosis and autophagy (*Cep131, Birc6, Thsd1*). Collectively, this gene profile might be expected to consolidate an inflammation and injury micro-environment in the NTS. Downregulation of genes required for normal axon circuit maintenance (*Fat1, Fat3, Myo10, Nav1, Dync1h1*) was again evident at day 28, and this was accompanied by a reduction in genes important for synaptic maintenance (*Dnmt3a, Csmd1, Csmd2, Urb4*), suggesting a disruption of normal network organisation in the NTS at this time point. Strikingly, day 28 NTS pathology may extend to include disruption of blood brain barrier function as several essential genes needed for blood brain barrier integrity were reduced, including genes encoding proteins involved in drug efflux and solute carriers (A*bcb1a, Slc2a1*) and endothelial tight junction formation (*Cldn5, Esam, Podxl*). This interpretation is also consistent with emerging evidence from other pulmonary injury paradigms that inflammatory spill-over from the lung can disrupt brain barrier integrity and contribute to neurological dysfunction (24). At the pathway level, day 28 changes were marked by positive enrichment of mitochondrial and energy-generating processes and negative enrichment of synaptic organisation, neuronal guidance, and cell adhesion-related categories, consistent with a more sustained disruption of neural circuit maintenance and functional integrity within the NTS.

Functional impacts of ALI neuroinflammation

The dramatic changes in the transcriptional landscape in the NTS following induction of ALI in this model are accompanied by measurable neurophysiological deficits. The NTS is an important component of brainstem circuitry involved in the regulation of breathing and airway reflexes (25, 51, 52). Consistent with this, basal breathing patterns were demonstrably different in vehicle-treated control versus bleomycin-treated rats. Although a role for peripheral mechanisms relating to the lung injury and changes in pulmonary physiology or gas-exchange cannot be discounted, the injury and inflammation in the NTS may also contribute to respiratory distress. In this regard, lung volume-sensing vagal sensory inputs to the NTS reflexively regulate breathing under basal conditions, while other sensory fibres can be recruited by lung inflammation and irritation to evoke defensive respiratory reflexes that are also dependent on NTS circuitry (25, 53–55). Indeed, Jacono and colleagues showed in a rat bleomycin model of ALI that acute breathing pattern changes were associated with rapid induction of IL-1b in NTS neurons (10). Consequently, changes in the efficacy of processing and relaying these inputs into brainstem respiratory network would conceivably change breathing patterning during ALI.

Further evidence that NTS processing is altered in bleomycin-induced ALI comes from direct neurophysiological assessments. Prior studies have reported that bleomycin lung-injury depresses

glutamatergic synaptic transmission in the NTS in neonatal rats (14). Thus, 7 days following bleomycin instillation, *ex vivo* electrophysiological recordings from NTS neurons in rat brainstem slices showed blunted excitatory potentials following vagal sensory nerve terminal stimulation, effects mediated by an increase in postsynaptic glutamatergic AMPA receptor isoforms that are impermeable to calcium. Intriguingly, our RNAseq data identified significantly upregulated expression of the AMPA receptor subunit 2, encoded by *Gria2*, which is subject to RNA editing within the second transmembrane domain rendering the channel impermeable to calcium (56, 57). Thus, our expression data also support a role for disordered NTS glutamatergic signalling, at least in the early stages of establishing the functional deficits observed later. Due to the deterioration in the health of the rats at day 7, *in vivo* functional experiments were not feasible at this time point in our study. However, at day 28, we performed *in vivo* NTS microinjections using either capsaicin (to stimulate neurotransmitter release from the central terminals of vagal sensory neurons) or a glutamate analogue (to directly activate NTS neurons independent of sensory inputs). These experiments revealed significantly blunted reflex respiratory responses, suggesting that the synaptic alterations observed early in ALI induction may persist, in some form, at later time points.

Limitations

Despite providing a comprehensive characterisation of brainstem molecular, cellular and functional changes following bleomycin-induced lung injury, this study has several limitations. First, it is primarily descriptive and does not directly resolve the mechanistic pathway by which lung injury signals to the brainstem. Although the NTS is a major central target of pulmonary vagal afferents, the present experiments cannot distinguish whether the observed neuroinflammatory changes are driven predominantly by vagal signalling, circulating inflammatory mediators, altered blood gases, or a combination of these mechanisms. Second, the RNA sequencing was performed on bulk NTS tissue, meaning that the detected transcriptional changes cannot be assigned to specific cell populations. Consequently, it remains unclear to what extent the altered expression profiles reflect neuronal, microglial, endothelial, astrocytic or other cellular responses within the region. Third, in vivo functional studies were only feasible at day 28, preventing direct linkage of the earlier transcriptional and microglial changes at day 7 with physiological dysfunction at that stage. Finally, the study uses a single bleomycin-induced model of acute lung injury, and therefore the generalisability of these findings to other causes of acute lung inflammation remains to be established. Nevertheless, the combined transcriptomic, morphometric and physiological data provide clear evidence that acute lung injury is sufficient to induce sustained pathology within the NTS and establish a foundation for future mechanistic and cell type-resolved studies of lung-brain signalling.

Conclusions

Our findings broaden the current understanding of how lung injury influences viscerosensory processing within the brainstem and offer new insights into potential mechanisms underlying the diverse neurological presentations frequently associated with ALI. The observed neuroinflammation and the

resulting functional hyposensitivity in the NTS may be related, in part, to microglial activation, as drugs targeting microglia (e.g., minocycline) have shown efficacy in the bleomycin lung model (14, 58). However, the precise mechanisms through which lung inflammation triggers microglial activation remain incompletely understood. Nevertheless, our data extend the understanding of the early pathophysiological signalling in the NTS, identifying novel signalling pathways that may contribute to the initiation and maintenance of the neuroinflammatory state. Additionally, we provide the first evidence of the pathophysiological evolution of NTS neuroinflammation, marked by later-stage disordered synaptic biology, neural circuit maintenance and blood brain barrier integrity. Future studies targeting these novel signalling pathways, either early or later in the disease model, may prove effective in modulating the neurological impacts of ALI and potentially translate into effective treatments that reduce the neurological complications in patients with lung injury.

Abbreviations

ALI
Acute lung injury
AMPA
α-amino-3-hydroxy-5-methyl-4-isoxazolepropionic acid
ARDS
Acute respiratory distress syndrome
BALF
Bronchoalveolar lavage fluid
BBB
Blood-brain barrier
BW
Body weight
CAMs
Cell adhesion molecules
cAMP
Cyclic adenosine monophosphate
cGMP
Cyclic guanosine monophosphate
CNS
Central nervous system
CT
Computed tomography
CTGF
Connective tissue growth factor
DEGs
Differentially expressed genes

EF50
Expiratory flow at 50% expired volume
FDR
False discovery rate
GSEA
Gene set enrichment analysis
GO
Gene Ontology
GO
BP:Gene Ontology biological process
IBA1
Ionised calcium-binding adaptor molecule 1
i.p.
Intraperitoneal
i.t.
Intratracheal
IL-1β
Interleukin 1 beta
IL-4
Interleukin 4
IL-6
Interleukin 6
LGA
L-glutamic acid
logCPM
Log counts per million
logFC
Log fold change
MDS
Multi-dimensional scaling
MD
Mean-difference
microCT
Micro-computed tomography
MV
Minute volume
NES
Normalised enrichment score
NeuN
Neuronal nuclei

NHMRC
National Health and Medical Research Council
NTS
Nucleus of the solitary tract
OCT
Optimal Cutting Temperature compound
PAU
Pause
Pa5
Paratrigeminal nucleus
PBS
Phosphate-buffered saline
PDE10A
Phosphodiesterase 10A
PEF
Peak expiratory flow
Penh
Enhanced pause
PFA
Paraformaldehyde
PIF
Peak inspiratory flow
qPCR
Quantitative polymerase chain reaction
RBC
Red blood cells
ROI
Region of interest
Rpef
Fraction of expiration at which peak expiratory flow occurs
RNAseq
RNA sequencing
SEM
Standard error of the mean
TB
Duration of breaking
Te
Expiratory time
Ti
Inspiratory time

TMM
Trimmed mean of M-values
TNFα
Tumour necrosis factor alpha
TP
Duration of pause before expiration
Tr
Relaxation time
TV
Tidal volume
WBP
Whole-body plethysmography

Declarations

Ethics approval and consent to participate: All animal procedures were approved by the Animal Ethics Committee of the University of Melbourne, Australia (approval number 2022-20038-25119-8), and were performed in accordance with the Australian Code for the Care and Use of Animals for Scientific Purposes.

Consent for publication: Not applicable.

Availability of data and materials: The RNA sequencing datasets generated during the current study are available in the [repository name] repository, [link/accession]. RNA-seq sample quality-control metrics, full differential expression tables from the limma-voom analysis, and full Gene Ontology biological process (GO:BP) ranked gene set enrichment analysis (GSEA) output tables for day 7 and day 28 are provided in the supplementary material.

Competing interests: The authors declare that they have no competing interests.

Funding: This work was funded by grants to A.E.M. from the Rebecca L. Cooper Medical Foundation and the Australian Research Council [DE230101079].

Authors' contributions: A.R.P., R.B., E.M.W., T.G.B., M.W.T. and A.E.M. performed and analysed experiments. S.B.M., G.P.A. and A.E.M. interpreted the data. S.B.M. and A.E.M. conceived the study, supervised the work and drafted the manuscript. All authors revised the manuscript and approved the final version.

Acknowledgements: The authors acknowledge the use of the services and facilities at the Australian Genome Research Facility (AGRF).

Authors' information: Not applicable.

References

1. Manicone AM. Role of the pulmonary epithelium and inflammatory signals in acute lung injury. Expert Rev Clin Immunol. 2009;5(1):63–75.
2. Bhatia M, Zemans RL, Jeyaseelan S. Role of chemokines in the pathogenesis of acute lung injury. Am J Respir Cell Mol Biol. 2012;46(5):566–72.
3. Ware LB, Matthay MA. The acute respiratory distress syndrome. N Engl J Med. 2000;342(18):1334–49.
4. Matuschak GM, Lechner AJ. Acute lung injury and the acute respiratory distress syndrome: pathophysiology and treatment. Mo Med. 2010;107(4):252–8.
5. Kaelberer MM, Caceres AI, Jordt SE. Activation of a nerve injury transcriptional signature in airway-innervating sensory neurons after lipopolysaccharide-induced lung inflammation. Am J Physiol Lung Cell Mol Physiol. 2020;318(5):L953–64.
6. Verzele NAJ, Chua BY, Law CW, Zhang A, Ritchie ME, Wightman O, et al. The impact of influenza pulmonary infection and inflammation on vagal bronchopulmonary sensory neurons. FASEB J. 2021;35(3):e21320.
7. Verzele NAJ, Chua BY, Short KR, Moe AAK, Edwards IN, Bielefeldt-Ohmann H, et al. Evidence for vagal sensory neural involvement in influenza pathogenesis and disease. PLoS Pathog. 2024;20(4):e1011635.
8. Le DD, Rochlitzer S, Fischer A, Heck S, Tschernig T, Sester M, et al. Allergic airway inflammation induces the migration of dendritic cells into airway sensory ganglia. Respir Res. 2014;15(1):73.
9. McSwiggin H, Wang R, Magalhaes RDM, Zhu F, Doherty TA, Yan W, et al. Comprehensive sequencing of the lung neuroimmune landscape in response to asthmatic induction. Front Immunol. 2025;16:1518771.
10. Jacono FJ, Mayer CA, Hsieh YH, Wilson CG, Dick TE. Lung and brainstem cytokine levels are associated with breathing pattern changes in a rodent model of acute lung injury. Respir Physiol Neurobiol. 2011;178(3):429–38.
11. Getsy PM, Mayer CA, MacFarlane PM, Jacono FJ, Wilson CG. Acute lung injury in neonatal rats causes postsynaptic depression in nucleus tractus solitarii second-order neurons. Respir Physiol Neurobiol. 2019;269:103250.
12. Hsieh YH, Litvin DG, Zaylor AR, Nethery DE, Dick TE, Jacono FJ. Brainstem inflammation modulates the ventilatory pattern and its variability after acute lung injury in rodents. J Physiol. 2020;598(13):2791–811.
13. Litvin DG, Denstaedt SJ, Borkowski LF, Nichols NL, Dick TE, Smith CB, et al. Peripheral-to-central immune communication at the area postrema glial-barrier following bleomycin-induced sterile lung injury in adult rats. Brain Behav Immun. 2020;87:610–33.
14. Litvin DG, Dick TE, Smith CB, Jacono FJ. Lung-injury depresses glutamatergic synaptic transmission in the nucleus tractus solitarii via discrete age-dependent mechanisms in neonatal rats. Brain Behav

Immun. 2018;70:398–422.

15. Yegen CH, Marchant D, Bernaudin JF, Planes C, Boncoeur E, Voituron N. Chronic pulmonary fibrosis alters the functioning of the respiratory neural network. Front Physiol. 2023;14:1205924.
16. Dusedau HP, Steffen J, Figueiredo CA, Boehme JD, Schultz K, Erck C, et al. Influenza A Virus (H1N1) Infection Induces Microglial Activation and Temporal Dysbalance in Glutamatergic Synaptic Transmission. mBio. 2021;12(5):e0177621.
17. Hosseini S, Wilk E, Michaelsen-Preusse K, Gerhauser I, Baumgartner W, Geffers R, et al. Long-Term Neuroinflammation Induced by Influenza A Virus Infection and the Impact on Hippocampal Neuron Morphology and Function. J Neurosci. 2018;38(12):3060–80.
18. Lemcke R, Egebjerg C, Berendtsen NT, Egerod KL, Thomsen AR, Pers TH et al. Molecular consequences of peripheral Influenza A infection on cell populations in the murine hypothalamus. Elife. 2023;12.
19. Mikkelsen ME, Christie JD, Lanken PN, Biester RC, Thompson BT, Bellamy SL, et al. The adult respiratory distress syndrome cognitive outcomes study: long-term neuropsychological function in survivors of acute lung injury. Am J Respir Crit Care Med. 2012;185(12):1307–15.
20. Radke J, Meinhardt J, Aschman T, Chua RL, Farztdinov V, Lukassen S, et al. Proteomic and transcriptomic profiling of brainstem, cerebellum and olfactory tissues in early- and late-phase COVID-19. Nat Neurosci. 2024;27(3):409–20.
21. Ma Q, Yao C, Wu Y, Wang H, Fan Q, Yang Q, et al. Neurological disorders after severe pneumonia are associated with translocation of endogenous bacteria from the lung to the brain. Sci Adv. 2023;9(42):eadi0699.
22. Jozefowicz RF. Neurologic manifestations of pulmonary disease. Neurol Clin. 1989;7(3):605–16.
23. Xu D, Zhao M, Liu G, Zhu T, Cai Y, Murayama R, et al. The vagus nerve-dependent lung-brain axis mediates brain demyelination following acute lung injury. Brain Behav Immun Health. 2025;44:100966.
24. Yu X, Xiao H, Bao S, Dong Y, Dong Z, Zhao J, et al. Cigarette smoke-induced lung-brain barrier dysfunction drives neurocognitive impairment via inflammatory spill-over. J Neuroinflammation. 2025;23(1):10.
25. Mazzone SB, Undem BJ. Vagal Afferent Innervation of the Airways in Health and Disease. Physiol Rev. 2016;96(3):975–1024.
26. Bassi JK, Connelly AA, Butler AG, Liu Y, Ghanbari A, Farmer DGS, et al. Analysis of the distribution of vagal afferent projections from different peripheral organs to the nucleus of the solitary tract in rats. J Comp Neurol. 2022;530(17):3072–103.
27. Deng X, Xiong X, Liu Y, Jia S, Wang F, Guo X, et al. Cognitive dysfunction in patients with interstitial lung disease. Front Med (Lausanne). 2026;13:1739386.
28. Vastag Z, Tudorache E, Traila D, Ciortea I, Fira-Mladinescu O, Oancea C et al. Neurocognitive Dysfunction in Fibrosing Interstitial Lung Diseases: A Multidimensional Analysis of Pulmonary, Cognitive, and Clinical Correlates. Diagnostics (Basel). 2025;16(1).

29. Mazzone SB, Bautista TG, Verberne AJM, Trewella MW, Farrell MJ, McGovern AE. Descending Modulation of Laryngeal Vagal Sensory Processing in the Brainstem Orchestrated by the Submedius Thalamic Nucleus. J Neurosci. 2020;40(49):9426–39.
30. Liu R, Holik AZ, Su S, Jansz N, Chen K, Leong HS, et al. Why weight? Modelling sample and observational level variability improves power in RNA-seq analyses. Nucleic Acids Res. 2015;43(15):e97.
31. Law CW, Chen Y, Shi W, Smyth GK. voom: Precision weights unlock linear model analysis tools for RNA-seq read counts. Genome Biol. 2014;15(2):R29.
32. Elizarraras JM, Liao Y, Shi Z, Zhu Q, Pico AR, Zhang B. WebGestalt 2024: faster gene set analysis and new support for metabolomics and multi-omics. Nucleic Acids Res. 2024;52(W1):W415–21.
33. Berg S, Kutra D, Kroeger T, Straehle CN, Kausler BX, Haubold C, et al. ilastik: interactive machine learning for (bio)image analysis. Nat Methods. 2019;16(12):1226–32.
34. Green TRF, Murphy SM, Rowe RK. Comparisons of quantitative approaches for assessing microglial morphology reveal inconsistencies, ecological fallacy, and a need for standardization. Sci Rep. 2022;12(1):18196.
35. Schindelin J, Arganda-Carreras I, Frise E, Kaynig V, Longair M, Pietzsch T, et al. Fiji: an open-source platform for biological-image analysis. Nat Methods. 2012;9(7):676–82.
36. McGovern AE, Driessen AK, Simmons DG, Powell J, Davis-Poynter N, Farrell MJ, et al. Distinct brainstem and forebrain circuits receiving tracheal sensory neuron inputs revealed using a novel conditional anterograde transsynaptic viral tracing system. J Neurosci. 2015;35(18):7041–55.
37. Kadam AH, Schnitzer JE. Characterization of acute lung injury in the bleomycin rat model. Physiol Rep. 2023;11(5):e15618.
38. Moeller A, Ask K, Warburton D, Gauldie J, Kolb M. The bleomycin animal model: a useful tool to investigate treatment options for idiopathic pulmonary fibrosis? Int J Biochem Cell Biol. 2008;40(3):362–82.
39. Liu T, De Los Santos FG, Phan SH. The Bleomycin Model of Pulmonary Fibrosis. Methods Mol Biol. 2017;1627:27–42.
40. Kolb P, Upagupta C, Vierhout M, Ayaub E, Bellaye PS, Gauldie J et al. The importance of interventional timing in the bleomycin model of pulmonary fibrosis. Eur Respir J. 2020;55(6).
41. Mouradian GC Jr., Alvarez-Argote S, Gorzek R, Thuku G, Michkalkiewicz T, Wong-Riley MTT, et al. Acute and chronic changes in the control of breathing in a rat model of bronchopulmonary dysplasia. Am J Physiol Lung Cell Mol Physiol. 2019;316(3):L506–18.
42. Hedley KE, Gomez HM, Kecelioglu E, Carroll OR, Jobling P, Horvat JC, et al. Neonatal Chlamydia muridarum respiratory infection causes neuroinflammation within the brainstem during the early postnatal period. J Neuroinflammation. 2024;21(1):158.
43. Beker MC, Altintas MO, Dogan E, Bayraktaroglu C, Balaban B, Ozpinar A, et al. Inhibition of phosphodiesterase 10A mitigates neuronal injury by modulating apoptotic pathways in cold-induced traumatic brain injury. Mol Cell Neurosci. 2024;131:103977.

44. Gross T, Stehle D, Nagel C, Zhou F, Duman E, Hernandez-Olmos V, et al. Inhibition of Phosphodiesterase 10A Alleviates Pain-like Behavior in Mice. Anesthesiology. 2025;142(2):332–48.
45. Huang J, Tang D, Cao Y, Wang Y, Long J, Wei L, et al. Inhibition of PDE10A-Rescued TBI-Induced Neuroinflammation and Apoptosis through the cAMP/PKA/NLRP3 Pathway. Evid Based Complement Alternat Med. 2022;2022:3311250.
46. Singh SP, Chhunchha B, Fatma N, Kubo E, Singh SP, Singh DP. Delivery of a protein transduction domain-mediated Prdx6 protein ameliorates oxidative stress-induced injury in human and mouse neuronal cells. Am J Physiol Cell Physiol. 2016;310(1):C1–16.
47. Pan J, Liu H, Zhou J, Liu Z, Yang Y, Peng Y, et al. Ipsilateral hippocampal proteomics reveals mitochondrial antioxidative stress impairment in cortical-lesioned chronic mild stressed rats. Curr Mol Med. 2014;14(9):1186–96.
48. Morikawa A, Hamase K, Inoue T, Konno R, Niwa A, Zaitsu K. Determination of free D-aspartic acid, D-serine and D-alanine in the brain of mutant mice lacking D-amino acid oxidase activity. J Chromatogr B Biomed Sci Appl. 2001;757(1):119–25.
49. Hashimoto A, Nishikawa T, Konno R, Niwa A, Yasumura Y, Oka T, et al. Free D-serine, D-aspartate and D-alanine in central nervous system and serum in mutant mice lacking D-amino acid oxidase. Neurosci Lett. 1993;152(1–2):33–6.
50. Widmer CA, Klebic I, Domanitskaya N, Decollogny M, Howald D, Siffert M, et al. Loss of the volume-regulated anion channel components LRRC8A and LRRC8D limits platinum drug efficacy. Cancer Res Commun. 2022;2(10):1266–81.
51. Kubin L, Alheid GF, Zuperku EJ, McCrimmon DR. Central pathways of pulmonary and lower airway vagal afferents. J Appl Physiol (1985). 2006;101(2):618–27.
52. Bonham AC, Chen CY, Sekizawa S, Joad JP. Plasticity in the nucleus tractus solitarius and its influence on lung and airway reflexes. J Appl Physiol (1985). 2006;101(1):322–7.
53. Canning BJ, Spina D. Sensory nerves and airway irritability. Handb Exp Pharmacol. 2009;194(194):139–83.
54. Chou YL, Scarupa MD, Mori N, Canning BJ. Differential effects of airway afferent nerve subtypes on cough and respiration in anesthetized guinea pigs. Am J Physiol Regul Integr Comp Physiol. 2008;295(5):R1572–84.
55. Bonham AC, Coles SK, McCrimmon DR. Pulmonary stretch receptor afferents activate excitatory amino acid receptors in the nucleus tractus solitarii in rats. J Physiol. 1993;464:725–45.
56. Sommer B, Kohler M, Sprengel R, Seeburg PH. RNA editing in brain controls a determinant of ion flow in glutamate-gated channels. Cell. 1991;67(1):11–9.
57. Melcher T, Maas S, Herb A, Sprengel R, Seeburg PH, Higuchi M. A mammalian RNA editing enzyme. Nature. 1996;379(6564):460–4.
58. Hong J, Adam RJ, Gao L, Hahka T, Xia Z, Wang D, et al. Macrophage activation in stellate ganglia contributes to lung injury-induced arrhythmogenesis in male rats. Acta Physiol (Oxf). 2021;232(2):e13657.

Figures

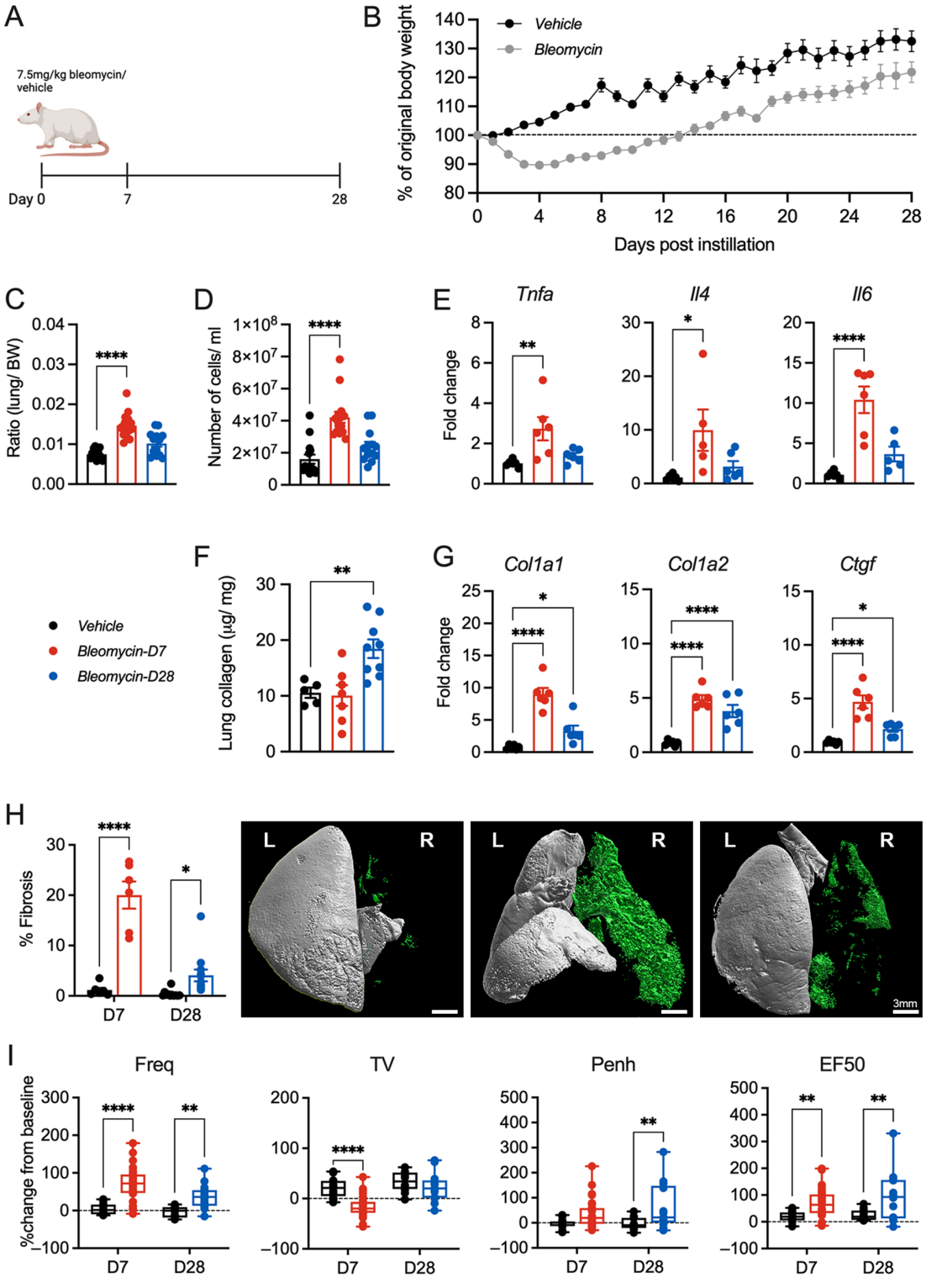


Figure 1

Characterisation of the rat model of bleomycin-induced lung injury. (A) Schematic demonstrating the experimental model where rats received either 7.5 mg/ kg bleomycin or vehicle (saline) via intratracheal administration (day 0) and euthanised at day 7 or day 28. Graphs depict (B) change in body weight, (C)

lung weight to body weight (BW) ratio, (D) total number of cells in bronchoalveolar lavage fluid, (E) fold change in expression of inflammatory (*Tnfa, Il4, Il6*) genes in the lungs, (F) total collagen levels determined by hydroxyproline assay in lungs and (G) fold change in expression of fibrotic (*Col1a1, Col1a2, Ctgf*) genes in the lungs at day 7 (orange) and day 28 (blue) post-bleomycin. The degree of lung pathologic changes was also assessed via (H) *ex vivo* micro-computed tomography (microCT) with quantification depicted in the graph and representative 3D scans showing bleomycin-induced lung injury in whole lungs obtained from vehicle, day 7 and day 28 rats (left to right). The left (L) lobe of the lung shows the microCT 3D volume image reconstruction in grey and the right (R) lobes demonstrate the segmented pathological regions in green identified via supervised machine learning analysis. Graphs (I) depict respiratory parameters (Freq, frequency; TV, tidal volume; Penh, enhanced pause; EF50, expiratory flow at 50 % expired volume) in vehicle- and bleomycin-treated rats, measured via whole body plethysmography. Graphical data are presented as mean ± SEM. *, **, **** denotes significance of $p < 0.05$, $p < 0.01$, $p < 0.0001$, respectively, as corrected for multiple comparisons and determined by (C) one-way ANOVA (Dunnett's), (D, E, F) Kruskal-Wallis test (Dunn's), (G) two-way ANOVA (Šídák), and (H) mixed effects model (Šídák).

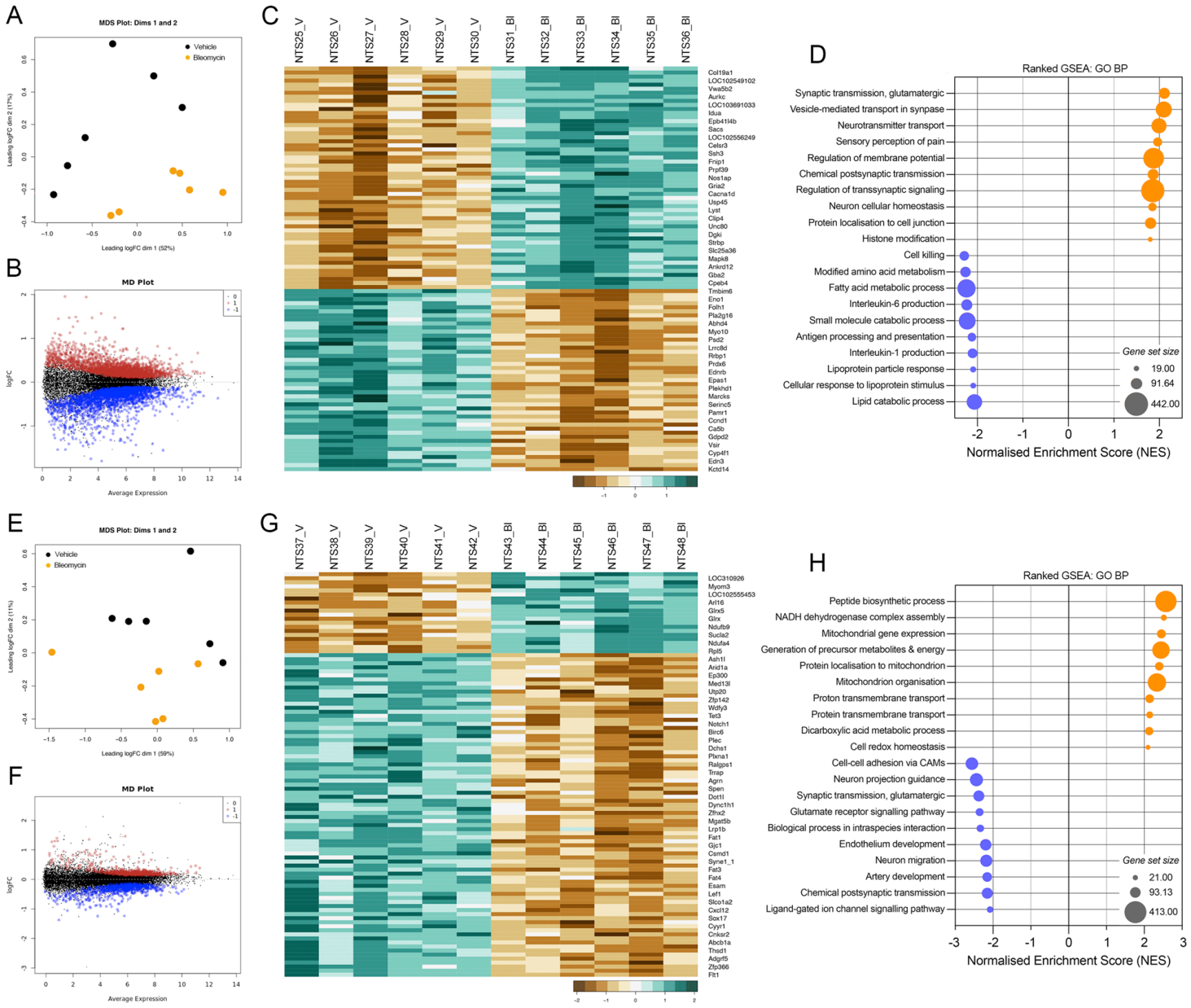


Figure 2

Nucleus of the solitary tract (NTS) transcriptional changes following bleomycin-induced lung injury. Multi-dimensional scaling (MDS) plot of batch-corrected logCPM values for NTS samples at (A) day 7 and (E) day 28 shows distinct clustering of samples from vehicle- (black) and bleomycin-treated (light brown) animals. Mean-difference (MD) plot showing gene-wise average log-expression versus log2-fold change for comparison between NTS from vehicle- and bleomycin-treated rats at (B) day 7 and (F) day 28 with significantly upregulated and downregulated genes in NTS bleomycin samples highlighted in red and blue, respectively. Heatmap of mean-adjusted logCPM values of the top 100 differentially expressed genes in NTS from vehicle-treated (V) and bleomycin-treated (Bl) rats at (C) day 7 and (G) day 28. For each gene listed, samples relatively high in its expression are coloured teal and samples relatively low in expression are coloured brown, while colour intensity represents the magnitude of the change. Ranked gene set enrichment analysis of Gene Ontology biological process (GO:BP) categories in NTS from

bleomycin-treated rats at (D) day 7 and (H) day 28. The plots show the selected top 10 positively enriched (orange) and top 10 negatively enriched (blue) GO:BP terms, displayed according to normalised enrichment score (NES), where positive NES values indicate enrichment toward the bleomycin-upregulated end of the ranked transcriptome and negative NES values indicate enrichment toward the bleomycin-downregulated end. Dot size represents gene set size. CAMs, cell adhesion molecules.

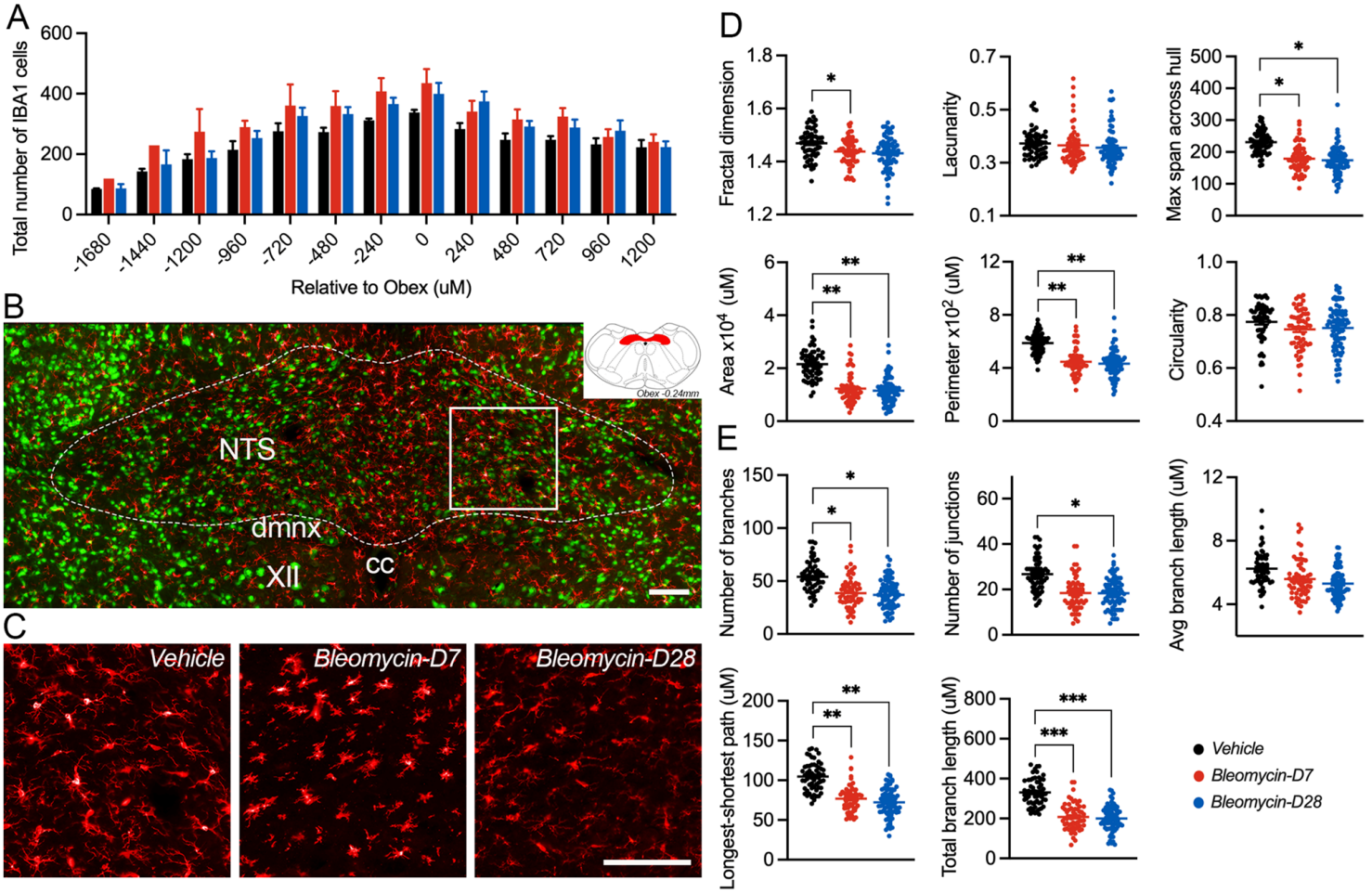


Figure 3

Morphometric changes in nucleus of the solitary tract (NTS) microglia following bleomycin-induced lung injury. (A) Quantification of IBA1-stained microglia across rostrocaudal levels (240 mM intervals) of the NTS in vehicle- (black; N=5) and bleomycin-treated rats (day 7, orange; N=4 and day 28, blue; N=5) rats. (B) Representative photomicrograph image of the NTS (dotted line demarcating the borders) and corresponding atlas line diagram (insert, red shading) at obex -0.24 mm, demonstrating the area used for subsequent single cell microglia morphometric analysis. The white box represents the vehicle-treated rat magnified image shown in panel C. Neurons are immunostained NeuN (green) and microglia immunostained with IBA1 (red). (C) Representative images showing IBA1-stained microglia in the NTS of vehicle- and bleomycin-treated rats at days 7 (Bleomycin-D7) and 28 (Bleomycin-D28). Dot plot graphs show (D) fractal analysis measuring the fractal dimension, lacunarity, maximum span across hull, area, perimeter, and circularity per microglial cell and (E) skeletal analysis measuring the number of branches,

number of junctions, average (Avg) branch length, longest to shortest path and total branch length. Data are presented as mean ± SEM. *, **, *** denotes significance of $p < 0.05$, $p < 0.01$, $p < 0.001$, respectively, as corrected for multiple comparisons and determined by either one-way ANOVA (Dunnett's) or Kruskal-Wallis test (Dunn's). cc, central canal; dmnx, dorsal motor nucleus of the vagus; NTS, nucleus of the solitary tract; XII, hypoglossal nucleus. Scale bar represents 100 mM.

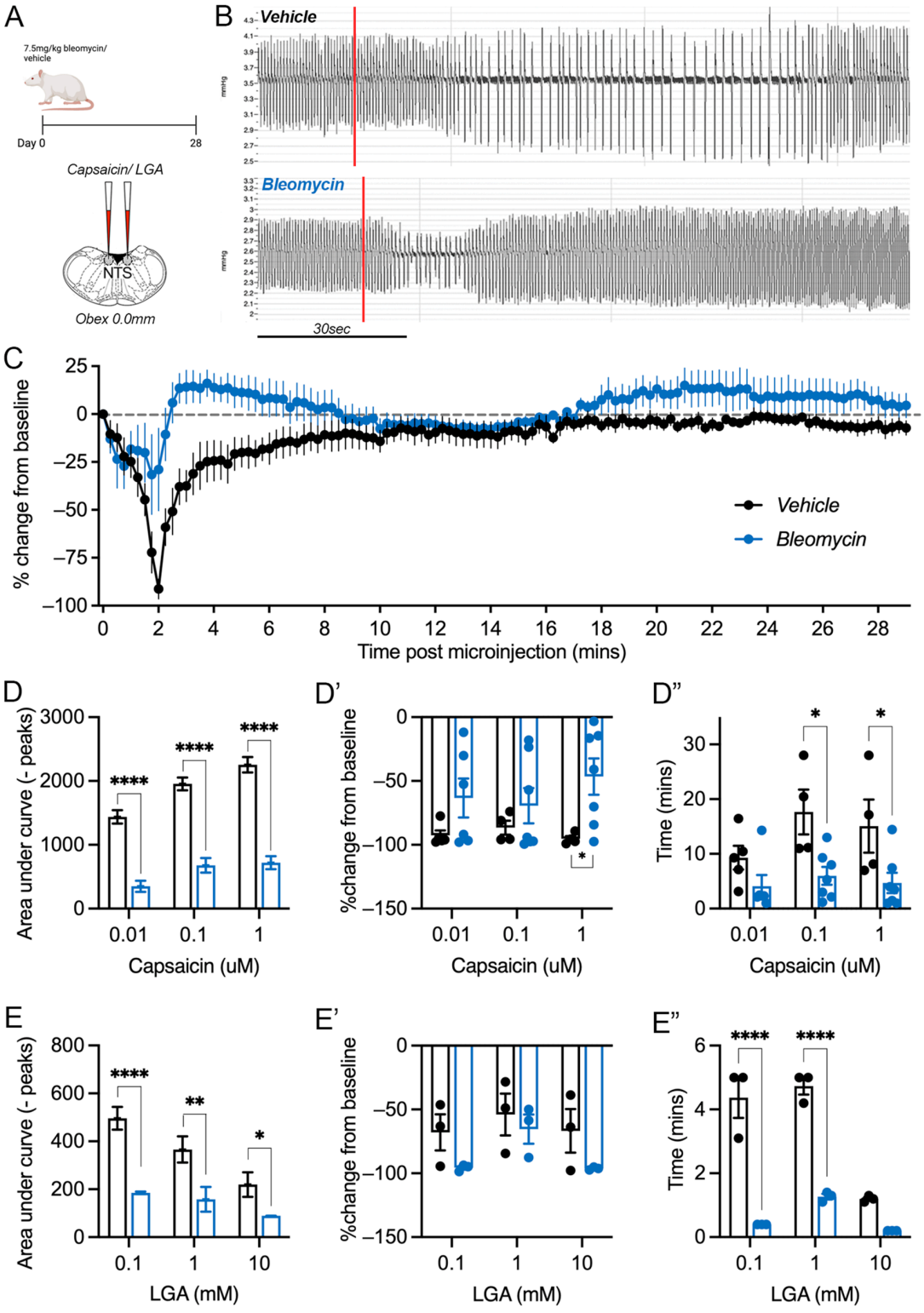


Figure 4

Changes in nucleus of the solitary tract (NTS) functional responsivity following bleomycin-induced lung injury. (A) Schematic of experimental design whereby rats that have received either vehicle or 7.5 mg/ kg bleomycin i.t., 28 days later undergo bilateral microinjections of either capsaicin or L-glutamic acid (LGA) into the NTS. (B) Representative chart traces showing respiratory movements after bilateral microinjection of capsaicin (red line) into the NTS from vehicle and bleomycin rats. (C) Example quantification of changes in respiratory frequency over the course of time following microinjection of 0.01 mM capsaicin into the NTS. Quantification of the changes in respiratory frequency represented by (D, E) area of negative peaks (area under the curve), (D', E') maximum response (D", E"), and time taken for respiratory rate to reach baseline (time to recovery) following increasing doses of capsaicin (0.01, 0.1, 1 mM) or LGA (0.1, 1, 10 mM), respectively. Data are presented as mean ± SEM. *, **, **** denotes significance of $p < 0.05$, $p < 0.01$, $p < 0.0001$, respectively, as corrected for multiple comparisons and determined by two-way ANOVA (Šídák).

Supplementary Files

This is a list of supplementary files associated with this preprint. Click to download.

- TableS1RNAseqQCmetrics.xlsx
- TableS2D7limmavoom.xlsx
- TableS3D28limmavoom.xlsx
- TableS4overlappinggenes.xlsx
- TableS5D7GSEAGOBP.xlsx
- TableS6D28GSEAGOBP.xlsx
- SupplementaryFigures.docx